3D-Architected Alkaline-Earth Perovskites

Jędrzej P. Winczewski,* Joel Arriaga Dávila, Manuel Herrera-Zaldívar,
Francisco Ruiz-Zepeda, R. Margoth Córdova-Castr, Camilo R. Pérez de la Vega,
Clément Cabriel, Ignacio Izeddin, Han Gardeniers,* and Arturo Susarrey-Arce*

3D ceramic architectures are captivating geometrical features with an immense demand in optics. In this work, an additive manufacturing (AM) approach for printing alkaline-earth perovskite 3D microarchitectures is developed. The approach enables custom-made photoresists suited for two-photon lithography, permitting the production of alkaline-earth perovskite ($BaZrO_3$, $CaZrO_3$, and $SrZrO_3$) 3D structures shaped in the form of octet-truss lattices, gyroids, or inspired architectures like sodalite zeolite, and C_{60} buckyballs with micrometric and nanometric feature sizes. Alkaline-earth perovskite morphological, structural, and chemical characteristics are studied. The optical properties of such perovskite architectures are investigated using cathodoluminescence and wide-field photoluminescence emission to estimate the lifetime rate and defects in $BaZrO_3$, $CaZrO_3$, and $SrZrO_3$. From a broad perspective, this AM methodology facilitates the production of 3D-structured mixed oxides. These findings are the first steps toward dimensionally refined high-refractive-index ceramics for micro-optics and other terrains like (photo/electro)catalysis.

1. Introduction

Perovskite is the trivial name of a category of significant compounds with crystal structures analogous to $CaTiO_3$. Perovskites are typically composed of alkali, alkali earth, or rare-earth (A), transition metal cations (B), and anions (X), usually oxide or halides.[1] Various forms and cation-pairings have been engineered or found in nature, in which the A-site cations generally have larger radii than B.[1] The simplest oxide perovskite is an ABX_3 with a cubic structure composed of BX_6 octahedra sharing corners with twelve-fold coordinated A sites located in the center of the cube of eight BX_6 units.[2] Beyond perfect perovskite crystals, distorted perovskites of reduced symmetries, such as triclinic, monoclinic, tetragonal, rhombohedral, and orthorhombic,[3] can be derived by combining A and B cations of particular ionic radii and electronegativity.[1] Within this construction, electronic structure and dipole moment can be altered by BX_6 octahedra tilting, which modifies the crystal field effect of the perovskite lattice, enabling their applicability in materials sciences.[4,5]

Among perovskites, alkaline-earth zirconates are attractive materials with functionality tunable by their chemical composition, for example, A = Sr, Ba, Ca, and B = Zr.[6,7] The added value of alkaline-earth zirconates can be found in emerging fields where materials scientists can contribute, like 3D micro-optics, light-emitting

J. P. Winczewski, J. Arriaga Dávila, H. Gardeniers, A. Susarrey-Arce
Mesoscale Chemical Systems
MESA+ Institute
University of Twente
P.O. Box 217, Enschede 7500 AE, The Netherlands
E-mail: j.p.winczewski@utwente.nl; j.g.e.gardeniers@utwente.nl;
a.susarreyarce@utwente.nl

M. Herrera-Zaldívar
Centro de Nanociencias y Nanotecnología
Universidad Nacional Autónoma de México
Km 107 Carretera Tijuana-Ensenada, Ensenada, Baja California, México
C.P. 22800, USA

F. Ruiz-Zepeda
National Institute of Chemistry
Hajdrihova 19, Ljubljana SI-1000, Slovenia

F. Ruiz-Zepeda
Department of Physics and Chemistry of Materials
Institute of Metals and Technology
Lepi pot 11, Ljubljana Slovenia

R. M. Córdova-Castr
Department of Physics
University of Ottawa
Ottawa, Ontario K1N 6N5, Canada

C. R. Pérez de la Vega, C. Cabriel, I. Izeddin
Institut Langevin
ESPCI Paris
CNRS
PSL University
1 rue Jussieu, Paris 75005, France

**ADVANCED
SCIENCE NEWS**

www.advancedsciencenews.com

**ADVANCED
MATERIALS**

www.advmat.de

devices, and photonic crystals, in which high-refractive index materials are much desired.[8] Among the alkaline-earth zirconates, $SrZrO_3$ has high dielectric permittivity and low microwave loss relevant for communication in small dielectric resonator antennas.[9] Other applications of $SrZrO_3$ include, for example, next-generation nonvolatile memory.[10] For other alkaline-earth zirconates, like $BaZrO_3$ and $CaZrO_3$, applications in wireless communication[11] and inorganic luminescent materials[12] can be found. From these examples, the alkaline-earth zirconates application range has gradually expanded and is expected to grow due to the demand for 3D ceramic microsystems.[8]

A commonwealth in $SrZrO_3$, $BaZrO_3$, and $CaZrO_3$ is the need for spatial organization, where cellular components of the specific composition are assembled and tailored to control chemical reaction performance or light–matter interaction. From this perspective, chemical technology is an important field where 3D architectures, like alkaline-earth zirconates, can also contribute. Alkaline-earth zirconates can then be geometrically designed catalysts to bridge between nanometer and micrometer length scales and act as a staircase to reach an understanding between chemical processes at the molecular level and the bulk continuum, where mass transport and diffusion might be rate-determining steps. Light-induced processes, such as photocatalysis, should not be excluded. In this case, 3D photocatalysts will require light management to modulate light–matter interaction (light absorption, reflection, and scattering) within a hierarchical architecture to promote carrier generation and induce chemical transformation, such as H_2 evolution from water splitting.[13]

Limited examples of alkaline perovskites exist in literature. These are scaffolds for bone regeneration,[14] piezoelectric,[15] and high-refractive index photonic crystals.[16,17] The lack of precursor versatility options is perhaps a potential reason for such limited examples. Like printed metal oxides, perovskites might suffer from particle-laden photoresists utilized in UV lithography, which is not applicable in such a realm. Under intense illumination, the dispersed particulate media strongly scatter light required for the photopolymerization, which exposes volumes higher than the desired voxel size. In turn, the resolution and attainable feature sizes are strongly compromised. Marino et al. have presented the additive manufacturing of composite piezoelectric microarchitectures printed using an Ormocomp-based photoresist with dispersed $BaZrO_3$ nanoparticles (10 wt%).[18] However, the authors have not studied the possibility of achieving solid ceramic 3D microarchitectures. Solid SiO_2 and ZrO_2 miniaturized replicas of the 3D microarchitectures have been achieved by using higher concentrations of nanoparticles (40–45 wt%) and thermal processing.[19,20] To circumvent the aggregation and provide dispersion stability, nanoparticles ($\approx$5–10 nm) can be either surface-functionalized or used along the binder matrix ($\approx$40 nm SiO_2 with hydroxyethyl methacrylate and trimethylolpropane ethoxylate triacrylate).[19–21]

Currently, the established method providing genuine 3D shaping of solid-beam metal oxide microarchitectures relies on tailored solutions for two-photon lithography (TPL).[22] Custom organic–inorganic photoresists are typically used to print metal-rich microarchitectures, subsequently annealed at elevated temperatures in the air to form self-miniaturized metal-oxide replicas. Examples of materials accomplished with the custom TPL-dedicated photoresists composed of organic–inorganic polymers

include TiO_2,[23] ZrO_2,[20,24] ZnO,[25] or SnO_2.[26] Recently, Bauer et al. presented the AM of nanoscale optical-grade glass architectures via a sinterless approach, utilizing a photoresist based on polyhedral oligomeric silsesquioxanes.[27] Reports on microarchitectures of more complex chemical composition often rely on the application of sol–gel photoresist based on a Si backbone, which permits the fabrication of, for example, mixed SiO_2 and ZrO_2,[28] or SiO_2 and TiO_2,[29] $SiOC$,[30,31] $SiCN$,[32] or $SiBCN$.[33] Alternatively, salts can be introduced to the photoresist to yield, that is, $Y_3Al_5O_{12}$,[34] or dope ZrO_2 with lanthanides.[24,35] The true uniqueness of such an approach is the possibility of tuning the chemical composition of resulting ceramics. From the previous examples, it is fair to say that there is an uttermost interest in elaborating solutions enabling the accurate structuring of complex oxide systems, like perovskites in 3D, to stimulate the thriving interfacing of material sciences in AM and overarch other science domains, like ceramic micro-optics.[8]

Although 3D-architected perovskites are attractive in various fields, an additional key limitation is derived from carbon-rich mixtures of organic–inorganic polymers used during printing. The TPL-dedicated photoresists demand precise precursor stoichiometry to reduce side product formation (i.e., non-stoichiometric mixtures, separated simple oxides) and reach the targeted alkaline-earth perovskite crystallographic phases.[36,37] In the zirconate synthesis, alkaline-earth oxide (AO) and ZrO_2 are first formed, desirably reacting to give the perovskite.[38] However, the AO may react with the CO_2 from the combusted organic components to give the carbonate.[38] Carbonate can endothermically decompose to CO_2 and AO,[39,40] and the latter can react with ZrO_2 to give the $AZrO_3$ perovskite (e.g., A = Ba, Ca, or Sr).[38] The decomposition activation energies, and in practice, decomposition temperatures, increase with the atomic number ($CaCO_3$ < $SrCO_3$ < $BaCO_3$) and depend on the crystalline carbonate form, which can end up varying the physical–chemical characteristics and structural architecture of the aimed 3D perovskite.[41] In addition, phase transitions of the components and impurities may occur throughout the annealing. Local chemical composition or morphological inhomogeneities can be expected throughout the material, especially if carbonate is buried or surrounded by perovskite. Our group has observed similar findings for low-temperature annealing ($\approx$600 °C) of ZrO_2, leading to buried carbon, which paradoxically increases the intrinsic mechanical properties of ZrO_2.[42] A way forward is to compensate for composition inhomogeneities; an excess amount of A-rich components, such as an excess of Sr, Ba, or Ca, is sometimes used to compensate for carbonate formation.[38,43]

To our knowledge, the AM of 3D perovskite architectures with sub-micrometer sizes has not yet been presented. Hence, this work introduces a library of 3D architected alkaline-earth zirconates of (sub-)micrometer sizes additively manufactured using tailor-made photoresists suitable with TPL. The 3D-printed organic–inorganic polymeric structures are thermally processed in the air at 1000 °C to eliminate the organic constituents and facilitate the formation of miniaturized replicas composed of, for example, $BaZrO_3$, $CaZrO_3$, and $SrZrO_3$ microarchitectures, denoted hereafter BZO, CZO, and SZO. The 3D ceramic microarchitectures and reference powders obtained from photoresists cured in bulk are investigated morphologically, structurally, and chemically. Insights into the optical properties of 3D printed
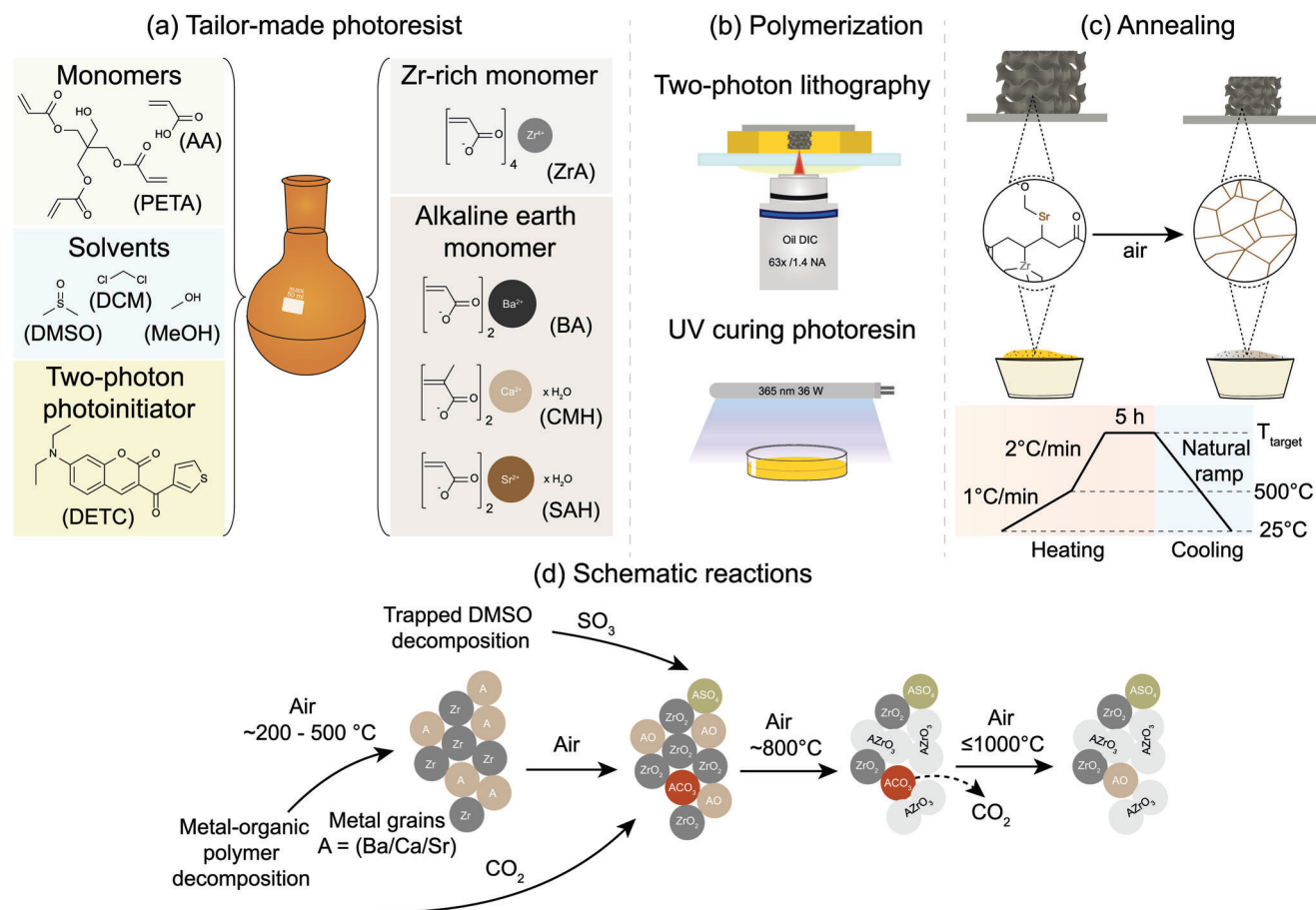
Figure 1. Additive manufacturing of BZO, CZO, and SZO 3D microarchitectures via TPL. a) Tailor-made photoresists combining ZrA, AA, PETA, and DETC dissolved in DMSO, MeOH, and DCM with BA, CMH, or SAH. b) 3D printing of the pre-ceramic 3D architectures (metal-containing polymers) on Si substrates using tailor-made photoresists or bulk using UV light. c) Annealing of the pre-ceramic 3D architectures and UV-cured photoresists to obtain miniaturized perovskite replicas and reference powders at 1 °C min^{-1} ramp to 500 °C, and 2 °C min^{-1} to the target temperature (T_{target} = 600, 700, 800, 900, or 1000 °C) with cooling at the natural ramp. d) Schematic representation of reactions—decomposition of metal–organic polymer yielding grains of Zr and alkaline-earth metal (A = Ba/Ca/Sr), which oxidize to the corresponding metal oxides—ZrO_2 or AO. The decomposition of organic constituents yields CO_2, which can form carbonates (ACO_3), and SO_3 formed via the combustion of trapped DMSO can react with AO to give ASO_4. While ACO_3 will likely decompose at 600–1000 °C, more stable ZrO_2 and ASO_4 with $AZrO_3$ as the main product will likely remain.

architectures are provided using cathodoluminescence and wide-field photoluminescence emission to estimate the lifetime rate and defects in $BaZrO_3$, $CaZrO_3$, and $SrZrO_3$. The freedom and integrability of 3D structuring can aid the accomplishment of ceramic structures composed of multiple elements, benefiting from TPL. From the AM scope, the results can pave the path for fabricating larger alkaline-perovskite architectures using conventional printing techniques, for example, stereolithography and digital light processing.

2. Results and Discussion

2.1. Additive Manufacturing of BZO, CZO, and SZO Architectures

The freedom of manufacturing a 3D perovskite library via TPL is showcased with different architectures. TPL photoresists are a key component that enables direct writing of the alkaline-earth perovskites (**Figure 1**). The process commences

with the preparation of the photoresists. The photoresists are prepared by dissolving zirconium acrylate (ZrA) and the respective alkaline-earth metal component, such as barium acrylate (BA), calcium methacrylate hydrate (CMH), or strontium acrylate hydrate (SAH) in dimethylsulfoxide (DMSO), methanol (MeOH) and acrylic acid (AA). The agents are combined with a crosslinker, pentaerythritol triacrylate (PETA), TPL photoinitiator, 7-diethylamino-3-thenoylcoumarin (DETC), and a small volume of dichloromethane (DCM) (Figure 1a). Upon complete dissolution, DCM and MeOH are removed under reduced pressure. The as-prepared resin is an orange-yellow mixture. Next, a photoresist droplet is cast onto a glass cover slide (Ø30 mm) and enclosed between two Kapton tape spacer ribbons, onto which a Si chip (8 × 8 mm) is placed. Underside, immersion oil is applied, and the substrate is mounted into a holder of a commercial TPL 3D printer (Photonic Professional GT, Nanoscribe) in a reflection configuration. The pre-ceramic 3D architectures (metal-containing polymers) are printed on Si dice and developed in DMSO and MeOH to clear away the non-polymerized photoresin
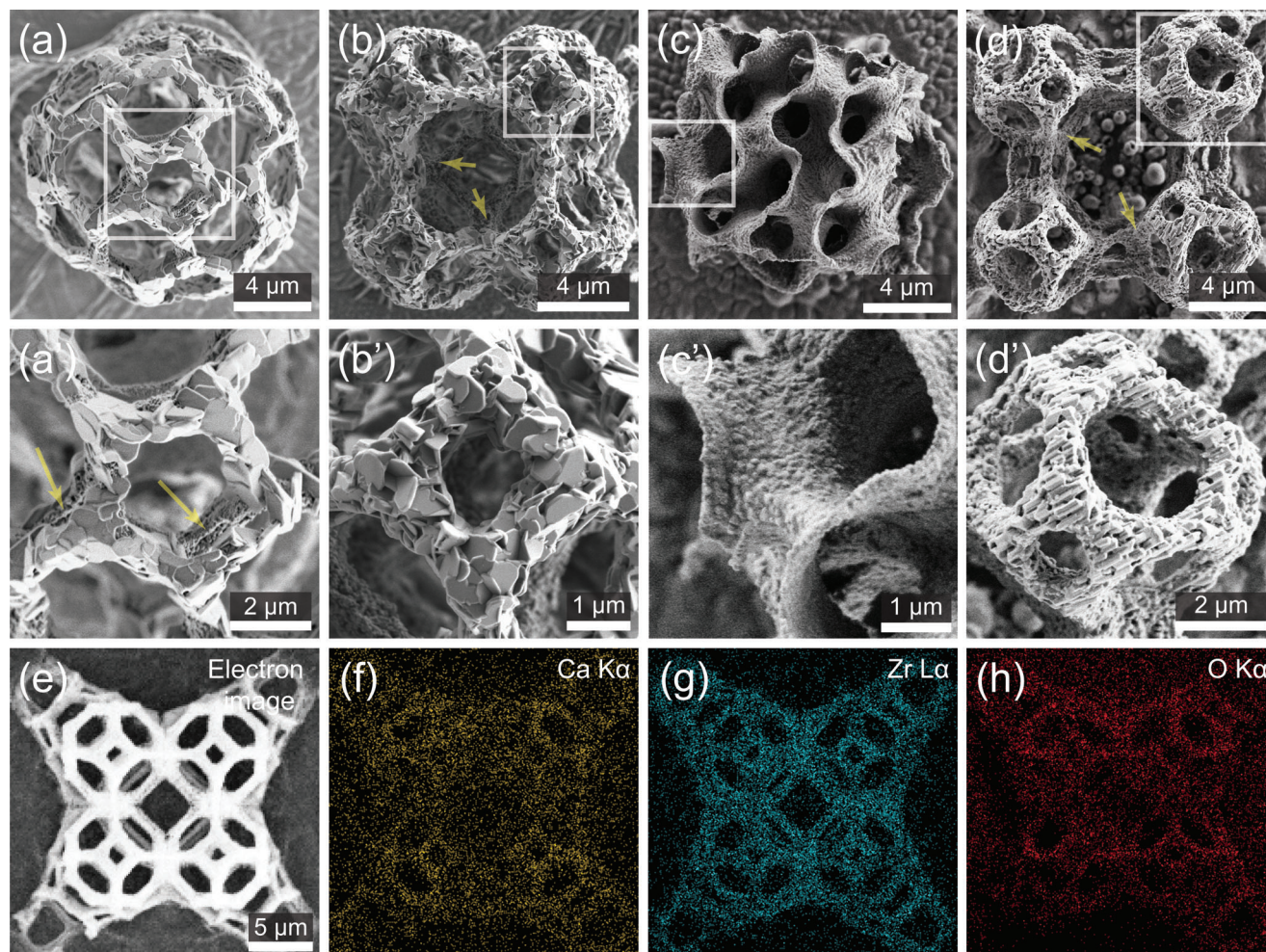
Figure 2. Morphological and chemical characteristics of the 3D BZO and CZO architectures. a–d) SEM images of BZO C_{60} buckyball-inspired architecture (a), BZO sodalite-inspired structure (b), CZO gyroid (c), and CZO zeolite sodalite-inspired structure (d). a′–d′) High-magnification SEM images of the areas indicated in the microscopy images (a–d). e) SEM–EDX mapping of the CZO sodalite-inspired structure presented in the electron image, and f–h) distribution of Ca (f), Zr (g), and O (h).

(Figure 1b and Section S1, Supporting Information). The structures are dried to remove traces of solvents, placed in the chamber oven, and annealed in atmospheric air at 1000 °C for 5 h. The 1 °C min^{-1} ramp to 500 °C and 2 °C min^{-1} ramp to the target temperature is applied to facilitate the combustion of organic constituents and the formation of metal grains, which are oxidized to yield metal oxides corresponding to the precursors used. The metal oxides mostly react to yield perovskites, though side-products may form (Figure 1d). For additional insights, readers are referred to Sections S2–S5, Supporting Information. A perovskite miniature replica of pre-polymeric structures is obtained (Figure 1c). UV-cured photoresists are annealed under the same conditions to obtain powder-like perovskite as reference powders. Depending on the photoresist composition, the BZO, CZO, and SZO can be obtained.

Scanning electron microscopy (SEM) images of the ceramic architectures are shown for BZO and CZO in **Figure 2** and SZO in **Figure 3**. SEM images of the corresponding pre-ceramic structures are presented (Figures S1 and S2, Supporting Information). SEM images of the reference powders annealed at the same tem-

perature as the architectures are shown in Figure S3, Supporting Information. For the BZO and CZO perovskites architectures in Figure 2, an isotropic shrinkage of ≈63% is observed upon annealing the pre-ceramic (Figure S1, Supporting Information). After calcination at 1000 °C, the BZO C_{60} buckyball-inspired structure (buckyball) and sodalite-inspired structure remain of similar geometry to the pre-ceramic structure. Regardless of the buckyball or sodalite design, the beams of BZO 3D structures primarily comprise outward-located disc-shaped grains of submicrometer widths, lengths, and thickness in the range of tens of nanometers (Figure 2a′,b′). The angled positioning of grains and foreshortening renders the measurement of their sizes imprecise based on the image analysis; thus, approximate values are not given. Interestingly, the disc-shaped grains fused in the beams resemble the macroscale Saharan gypsum desert rose morphology.[44] Within the same architectures, smaller grains are positioned in the central parts and neighboring large crystal edges (see yellow arrow highlight). Sintered crystals are also observed in Figure 2a′. The preferential external situation of large disc-shaped crystals may be associated with heat transfer and local temperature
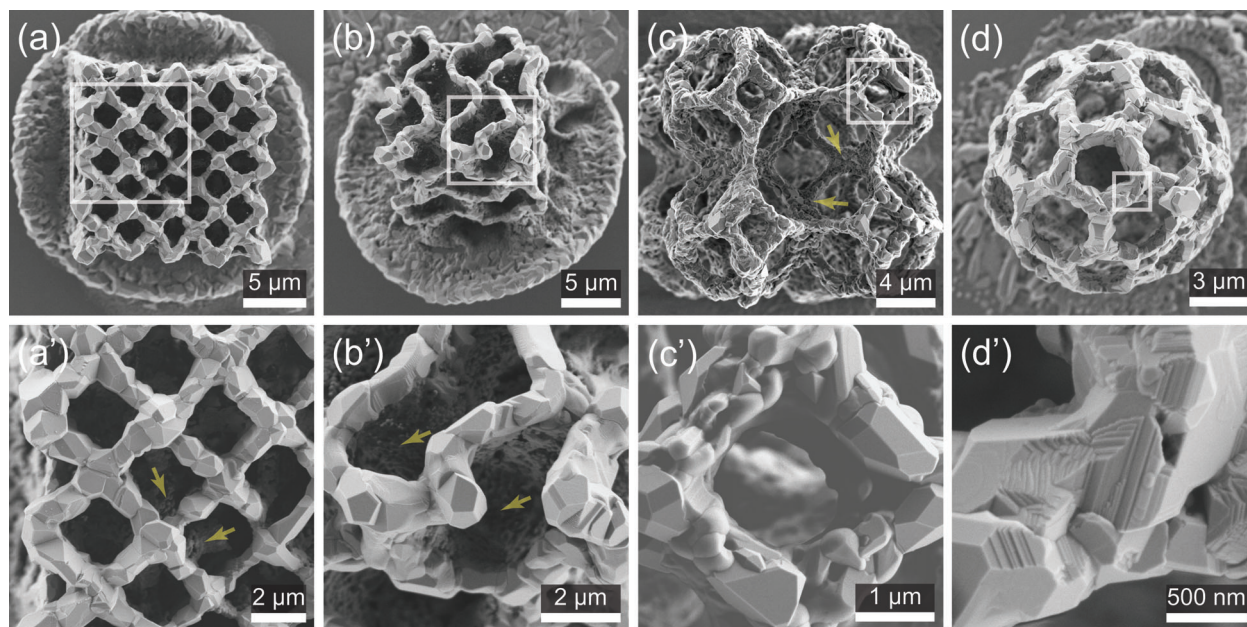
**ADVANCED
SCIENCE NEWS**

www.advancedsciencenews.com

**ADVANCED
MATERIALS**

www.advmat.de

Figure 3. Morphological characterization of the additively manufactured SZO 3D microarchitectures. a–d) SEM images of octet-truss lattice (a), gyroid (b), sodalite-inspired architecture (c), and C_{60} buckyball-inspired structure (d). a′–d′) High-magnification SEM images of the areas indicated in the microscopy images (a–d).

inhomogeneities throughout the 3D architectures during annealing, as computed and experimentally investigated in mm-lengthscale ceramics.[45]

The CZO gyroid (Figure 2c) comprises nanograins, more irregular than in BZO, with a width and length of ≈100–200 nm. The zeolite sodalite-inspired architecture (Figure 2d) has elongated oblong-like nanograins with approximate lengths of hundreds and widths of two hundred nanometers. A relation between the nanograin size and shape cannot yet be attributed to the architectural design. However, it can reasonably be related to the chemical composition of the perovskite architecture. For example, SZO (Figure 3) reveals larger crystals than BZO and CZO (Figure 2). Figure 2f–h demonstrates the elemental distribution of (f) Ca, (g) Zr, and (h) O, homogeneously allocated within the solid beams of the CZO sodalite-inspired architecture depicted in the SEM image (Figure 2e); no areas appear to be deficient in one of these elements, no hotspots are found.

The SZO shows isotropic shrinkage similar to the other alkaline-earth zirconates. Larger grains of lengths and widths close to the micrometer have been observed. The sintering is pronounced at the grain boundaries and the microarchitecture edges (Figure 3). Additionally, nanometric grains are observed in the central areas of the octet-truss lattice and gyroid, as highlighted by the yellow arrows in Figure 3a,b. Overall, SZO sharp-edge grains are smaller than in the gyroid and octet-truss lattice, and their size distribution is inhomogeneous. Even though the same annealing conditions are applied, these smaller grains are practically not noted in the more open architectures, like the sodalite-inspired structure (Figure 3c). The effect can be related to the structure type, which due to thermal transport during annealing, might vary across the closely packed architectures (octet-truss lattice and gyroid). Similar observations to the zeolite-inspired architecture can be made for the buckyball (Figure 3d), where

multiple steps can be observed in the buckyball on the grain surface (Figure 3d′). These steps may be correlated with edge dislocations, in which vectors appear to align along the buckyball beams. These are very important observations from the crystal growth standpoint. The chemical composition, annealing treatment, and the ratio between the volume occupied by the material and air within the 3D architecture are factors that influence the crystal growth process. Tailoring such parameters, we can produce a perfect 3D crystal hypothetically.

From the image inspection in Figures 2 and 3, the largest grains are obtained for SZO and the smallest for CZO. For BZO and SZO, the crystal growth and morphology appear to depend on the geometry and composition of the 3D pre-ceramic microarchitectures. The structural integrity of the BZO and SZO octet-truss lattices is assessed with focused ion beam (FIB) tomography (Videos S1 and S2, Supporting Information). The analysis reveals the inner polycrystalline microstructure. The SZO grains are densely packed, and voids are found within the BZO beams. In perspective, the future development of this TPL approach may open the possibility of growing crystals of specific chemical composition, morphology, size, or defects (i.e., point, line, or bulk defects) applicable for photocatalysis.[13,46,47] In retrospect, ultra-smooth crystals with fewer defects can facilitate light propagation with minimum losses, enabling the production of micro-optical components.

2.2. Structural Characteristics of BZO, CZO, and SZO

BZO, CZO, and SZO reference powders (Figure 1) are synthesized from the corresponding tailor-made photoresists to limit potential impurities and control the microarchitecture chemical composition. The prepared UV-cured pre-ceramic

photopolymers are pulverized and annealed in the crucibles at 600, 700, 800, 900, and 1000 °C for 5 h to yield white BZO, CZO, and SZO powders.

The X-ray powder diffraction (XRD) measurements for the BZO (Figure S4, Section S2.1., Supporting Information) feature the reflections distinctive of cubic phase barium zirconate (c-BaZrO$_3$).[35] The main identified impurity is orthorhombic barium sulfate (o-BaSO4), and minor amounts of monoclinic zirconia (m-ZrO$_2$) are found. In CZO powder synthesized from the equimolar amount of Ca- and Zr-rich monomers, besides orthorhombic calcium zirconate (o-CaZrO$_3$), a significant amount of impurities, for example, orthorhombic calcium sulfate (o-CaSO$_4$) and tetragonal zirconia (t-ZrO$_2$) are observed in Section S2.2., Supporting Information. The reference powders with Ca:Zr ratios 1:1, 1.1:1, 1.25:1, and 1.5:1 annealed at 1000 °C for 5 h are studied to improve product quality (Figure S5, Supporting Information). The excess Ca is required to promote CaZrO$_3$ synthesis since the least impurities and the highest CaZrO$_3$ content are achieved for the Ca:Zr ratio of 1.5:1. The Ca concentration is not increased further due to the limited CMH solubility. The CZO (at 1.5 to 1 Ca:Zr ratio) powders synthesized from the UV-cured photoresists annealed at 600, 700, 800, 900, and 1000 °C for 5 h are characterized (Figure S6, Supporting Information). At lower temperatures (600, 700, and 800 °C), large amounts of orthorhombic calcium sulfate (o-CaSO$_4$), calcium carbonate (CaCO$_3$), and tetragonal zirconia (t-ZrO$_2$) are found as impurities. The orthorhombic phase strontium zirconate (o-SrZrO$_3$) is identified for SZO (Figure S7, Supporting Information). Minor amounts of m-ZrO$_2$ and orthorhombic strontium sulfate (o-SrSO$_4$) are confirmed (Figure S7, Supporting Information). The ASO$_4$ (A = Ba, Ca, Sr) is related to the DMSO in the photopolymer (Figure 1).

In summary, XRD results for BZO show the characteristic features of c-BaZrO$_3$ upon annealing at 700 °C; the increased temperature improves crystallinity and reduces the general impurity content. In the case of CZO, at lower temperatures (600, 700, and 800 °C), large volumes of impurities are found, mostly suppressed after the treatment at 1000 °C. For SZO, reflections associated with o-SrZrO$_3$ are already detected for powders annealed at 600 °C. A significant volume of impurities is found through 600–900 °C. The annealing of SZO at 1000 °C results in SrZrO$_3$ with a minor impure phase volume. The lattice parameters of BZO, CZO, and SZO annealed at 1000 °C agree with the literature (Table S1, Supporting Information). On average, the treatment at 1000 °C yields the purest c-BaZrO$_3$, o-CaZrO$_3$, and o-SrZrO$_3$ perovskites (Figures S4, S6, and S7, Supporting Information); thus, it is selected as the annealing temperature for the 3D structures.

Complementary insights into impurities and surface composition of BZO, CZO, and SZO reference powders annealed for 5 h at 1000 °C are provided using X-ray photoelectron spectroscopy (XPS). The general survey reveals the presence of Ba, Zr, O, C, and S in BZO (Figure S8a, Supporting Information). The analysis of BZO core regions confirms that BaZrO$_3$ is synthesized and BaSO$_4$ and BaCO$_3$ impurities are found (Figure S8b–f, Supporting Information). For CZO, the general survey proves the presence of Ca, Zr, O, C, and S (Figure S9a, Supporting Information). The dominant product is CaZrO$_3$, accompanied by CaCO$_3$ and traces of CaSO$_4$ (Figure S9b–f, Supporting Information). Significantly more CaCO$_3$ is found in CZO than in BZO and SZO. The

analysis confirms that Sr, Zr, O, C, and S are present in SZO powder (Figure S10a, Supporting Information). The dominant component is SrZrO$_3$; similarly, SrCO$_3$ and SrSO$_4$ are detected as side-products (Figure S10b–f, Supporting Information). The species assigned with XPS are consistent with XRD analysis results.

Next, we analyze the chemical composition of the FIB-processed lamellae extracted from the BZO, CZO, and SZO microarchitectures. The results in **Figure 4** are accompanied by SEM–EDX (Figures S11–S14, Section S4, Supporting Information). The annular dark-field scanning transmission electron microscopy (ADF-STEM) images of lamellas are given in Figure 4a–c. The STEM-EDX mapping indicates the Ba, Zr, and O distribution throughout the BZO lamella in Figure 4a–a‴ with visible Ba hotspots. The selected area electron diffraction (SAED) pattern indicates the mixing of ZrO$_2$ and BaZrO$_3$ phases (Figure S15a, Supporting Information). The findings are well aligned with previously discussed XRD and XPS results. Further, electron energy loss spectroscopy (EELS) shows the presence of edges from Zr, O, and Ba, all collected from a single grain (Figure S15d, Supporting Information). Next, the CZO is analyzed. The fragile nature of CZO made it difficult to prepare and handle a lamella; thus, higher-magnification images are provided of the representative region; the EDX maps confirm the homogenous allocation of Ca, Zr, and O within the sampled area. The corresponding SAED pattern indicates the presence of CaZrO$_3$ and ZrO$_2$ (Figure S15b, Supporting Information). For SZO, EDX confirms a more homogenous distribution of Sr, Zr, and O within the area of interest in Figure 4c–c‴, correlating with the SAED pattern dominated by reflections for SrZrO$_3$ (Figure S15c, Supporting Information). No discernible ZrO$_2$ rings have been found. However, some diffraction spots with values close to ZrO$_2$ are observed. Although there are some small inhomogeneities, forming mixed-phase products and segregation is a known phenomenon for alkaline-earth perovskites.[48,49] The local inhomogeneities in the composition of BZO, CZO, and SZO microarchitectures can be additionally related to the bulk character of the pre-ceramic beams, hindering the formation of stoichiometric product within their cores. In addition, STEM imaging reveals the nanoporosity within the nanoporous character within the core of the material (see Figure S16, Supporting Information).

2.3. Optical Properties of BZO, CZO, and SZO

The optical properties of BZO, CZO, and SZO are evaluated. First, diffuse reflectance spectroscopy measurements are conducted for the BZO, CZO, and SZO powders (Section S7, Supporting Information). Using the Kubelka–Munk function and Tauc plot, 4.38, 3.81, and 4.31 eV, indirect transition bandgaps are determined for BZO, CZO, and SZO, respectively (Figure S17, Supporting Information).[50] The estimated values agree with the literature. The BZO bandgaps of 4.9–3.8 eV were reported for powders.[51,52] For reference, CZO 4.38–3.85 eV optical bandgaps were measured, and bandgaps of 4.1–3.3 eV were calculated.[53–55] SZO optical bandgap values ranging from 5.5 to 3.5 eV were previously stated, depending on the synthesis method and morphology.[13,56,57] The bandgaps of zirconates can be altered by the defects, that is, oxygen vacancies, strain,
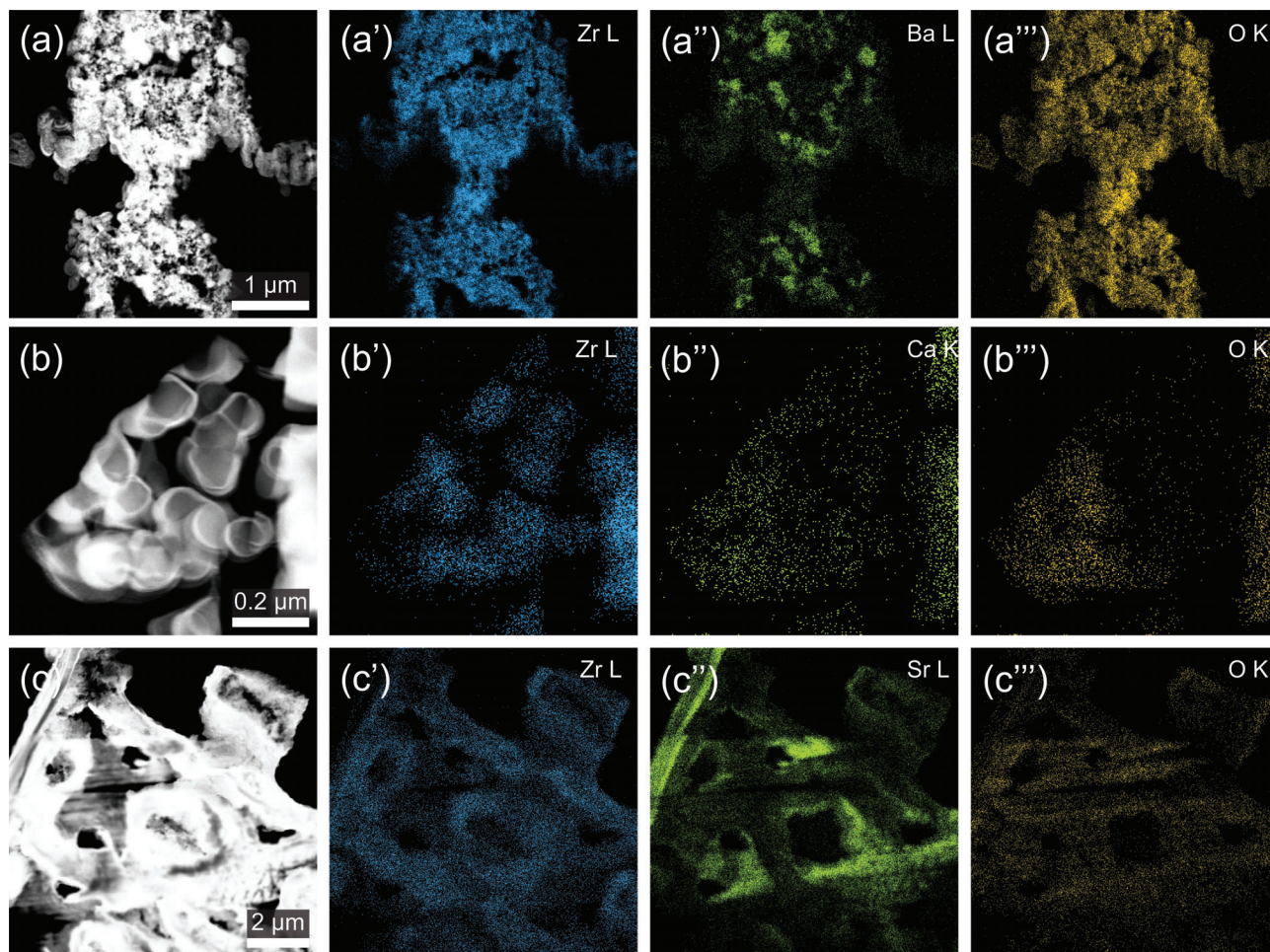
Figure 4. a–c) ADF-STEM images of BZO (a), CZO (b), and SZO (c) lamellas with corresponding EDX maps showing the distribution of Zr (a′–c′), alkaline-earth elements (a″–c″), and O (a‴–c‴) throughout the sampled areas.

and lattice mismatches.[55,58] Therefore, the nature of some defects is unraveled optically. Access to interrogate BZO, CZO, and SZO microarchitectures is nontrivial. First, cathodoluminescence (CL) measurements provide insights into the point defects and associated emissions. The CL spectra are deconvoluted into the peaks corresponding to defect-related emissions (**Figure 5**a–c). The corresponding panchromatic SEM–CL images resenting the emissions from the 3D microarchitectures are shown (Figure 5a″–c″). CL spectra for BZO, CZO, and SZO reference powders are presented in Figure S18, Supporting Information for comparison. During peak-fitting of Gaussian components, 0.35 eV full width at half maximum (FWHM) is set. FWHM manifests a homogenous and inhomogeneous widening of line widths related to electronic transitions. The coupling between electrons and phonons within perfect crystals results in homogenous peak widening, illustrated with the Lorentzian profile. The disorder, that is, impurities, vacancies, or anti-site defects, contributes to the inhomogeneous peak widening, portrayed with the Gaussian profile.[59,60]

First, the CL spectrum recorded for BZO microarchitectures is discussed. The Gaussian components are fitted at 1.7 (CL_I),

2.3 (CL_{II}), 2.6 (CL_{III}), 2.93 (CL_{IV}), 3.27 (CL_V), 3.57 (CL_{VI}), and 3.9 eV (CL_{VII}). The spectrum is dominated by CL_{IV} contribution, followed by high-intensity CL_{III} and CL_V signals. The intensity of medium-intensity CL_{II} and CL_V peaks is comparable, while CL_I and CL_{VII} are relatively weak. The observed broad-range emissions stem from a multiphonon, multilevel process, including various relaxation pathways.[61–63] The spectrum is a combination of emissions correlating with structural order–disorder of ZrO_5 and ZrO_6 clusters, distortion, dangling bonds, oxygen vacancies (V_O), singly ionized V_O ($V_O^\bullet$), or disorder in the BaO_{12} and ZrO_6 network.[51,62–65] The assignments of particular peaks in literature are often divergent and may differ depending on the synthesis method, particle morphology, size (e.g., nanometric or micrometric size), or crystallinity.[62] The emission ≈1.6–1.7 eV was previously assigned to the V_O in HfO_2, Hf^{4+}, or other transition elements, which trace amounts are often found in ZrO_2.[66,67] Cavalcante et al. used electron paramagnetic resonance (EPR) measurements to correlate the 2.3 eV emission with $V_O^\bullet$ associated with [ZrO_5] clusters.[51] The 2.6 eV emissions were reported to stem from the structural order–disorder governed by [ZrO_5] and [ZrO_6] clusters or [BaO_{12}] sites.[61,64,68] The 2.9 eV emissions correlate with the V_O, or singly ionized V_O ($V_O^\bullet$) associated with
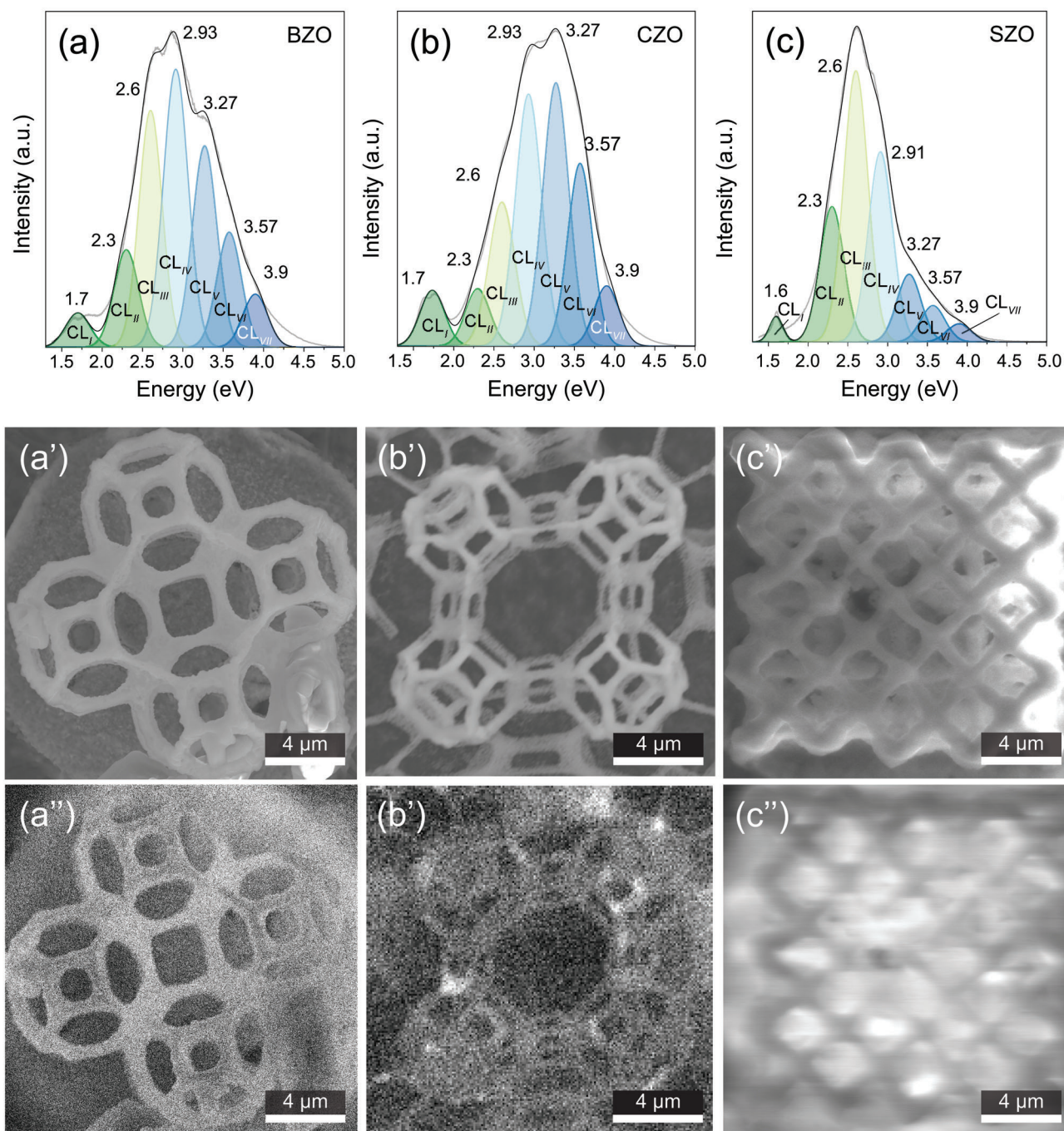
Figure 5. Deconvoluted CL spectra collected from the sodalite-inspired BZO (a) and the zeolite sodalite-inspired CZO (b) microarchitectures, and the octet-truss lattice SZO (c), and corresponding SEM (a′–c′) and panchromatic SEM–CL (a″–c″) images.

[ZrO$_5$] clusters.[62,69] The weak UV and violet emissions (3.9, 3.57, and 3.27 eV) correlate with shallow trap states.[70] Conversely, the peaks ≈3.29–3.44 eV were previously assigned to free exciton recombination.[64,71] Similar emissions have been observed for BZO reference powders in Figure S18a, Supporting Information. Interestingly, the 2.3 and 2.6 eV emissions are lower for the powder references than the 3D microarchitectures, indicating a lower degree of disorder for the powder samples. Additionally, BZO powder reveals the loss of the 3.9 eV emission previously assigned to shallow trap states. Besides the spatial organization offered by 3D printing, which can enable the control of (photo)chemical reaction performance[72,73] or light–matter interaction in optics and photonics.[22] Defective and disordered BZO 3D microarchitectures can be treated as oxygen-deficient systems, which hold important applications in electrochemistry. This is the case with lithium-ion batteries, where our BZO 3D

ADVANCED
SCIENCE NEWS
www.advancedsciencenews.com

**ADVANCED
MATERIALS**
www.advmat.de

microarchitectures might play a crucial role during anion-redox reactions.[74,75]

The CL spectrum collected from the CZO microarchitecture (Figure 5b) is deconvoluted into seven peaks at 1.7 (CL_I), 2.3 (CL_{II}), 2.6 (CL_{III}), 2.93 (CL_{IV}), 3.27 (CL_V), 3.57 (CL_{VI}), and 3.9 eV (CL_{VII}). The CL_I, CL_{II}, and CL_{VII} peaks are very weak. The CL_{IV} and CL_V components dominate the spectrum, while CL_{III} and CL_{VI} are medium-intensity. The data regarding luminescent properties of CZO is limited; nonetheless, its emissions were previously associated with V_O, $V_O^\bullet$, and the distorted Ca and Zr networks, with the resulting $[CaO_7 \cdot V_O^\bullet]$, $[CaO_7 \cdot V_O^{\bullet\bullet}]$, $[ZrO_5 \cdot V_O^\bullet]$ and $[ZrO_5 \cdot V_O^{\bullet\bullet}]$ centers.[76,77] Certain resemblances of CL spectra of BZO and CZO are present, indicating potential similarities of defects to which the emissions correlate. Furthermore, the deconvolution of the SZO CL spectrum gives seven Gaussian components, ranging from long-wave UV to red. The peaks are found at 1.6 (CL_I), 2.3 (CL_{II}), 2.6 (CL_{III}), 2.91 (CL_{IV}), 3.27 (CL_V), 3.57 (CL_{VI}), and 3.9 eV (CL_{VII}). The weak UV and violet emissions at $CL_{VII} - CL_{III}$ are associated with shallow defects within E_g, such as $[SrO_{11} \cdot V_O^\bullet]$ and $[SrO_{11} \cdot V_O^{\bullet\bullet}]$ clusters.[78–80] These also imply the off-stoichiometric material character.[81] The emissions ranging from green to red, for example, CL_I and CL_{II}, correlate with the deep E_g defects, such as $[ZrO_5 \cdot V_O^\bullet]$ and $[ZrO_5 \cdot V_O^{\bullet\bullet}]$.[78–80] Similar to BZO reference powders, CZO and SZO (Figure S18b,c, Supporting Information), the 2.3 and 2.6 eV emissions are reduced for the powder references than the 3D microarchitectures. Additionally, CZO and SZO powder reveal the loss of the 3.9 eV emission. Those characteristics are of importance in the field of reaction chemistry, such as photocatalysis.[72,73] Although BZO, CZO, and SZO reveal optically the presence of oxygen deficiencies, the optical response is attributed to local inhomogeneities in our alkaline-perovskite microarchitectures, we can expect that longer annealing times to reduce background emissions from defects for the production of refractive index ceramics in micro-optics.[8,28] Our group has observed similar findings for low-temperature annealing ($\approx$600 °C) of denser ZrO_2 ceramics,[24] which could have caused the buried of carbon or non-stochiometric components,[42] as could be the case for non-stoichiometric BZO, CZO, and SZO species.

Next, we evaluate the wide-field photoluminescence (PL) emission to estimate the lifetime rate of defects in the alkali-earth perovskite printed architectures. For BZO, the local emission maxima are recorded at $\approx$543 nm for excitation at 450 nm in Figure S19a, Supporting Information. In the case of CZO, excitation at 450 nm in emissions with local maxima $\approx$543 nm (Figure S19b, Supporting Information). For SZO, the highest PL emission intensity is observed at $\approx$571 nm upon excitation at 450 nm (Figure S19c, Supporting Information). The registered PL signals are excited at relatively low energies due to the availability of the optical systems. The registered PL spectra are limited to the signals corresponding to the cathodoluminescence emissions assigned to the CL_I, CL_{II}, CL_{III}, and CL_{IV} peaks associated with Vo and intrinsic metal-oxygen coordinated centers.

The photoluminescence (PL) decay rate histograms are obtained through time-correlated single-photon counting (TCSPC) measurements to understand the lifetime of excited states in alkaline-earth perovskites. The BZO, CZO, and SZO are excited with a 450 nm wide-field laser beam emitted by a supercontinuum laser using an inverted fluorescence microscope with a 20× objective. The PL emission is collected and focused onto a single photon avalanche diode coupled to a time-resolved photon counting module, with a 2.5 µm field of view and $\approx$200 ps instrument response function (IRF) temporal width using the measured fluorescence intensity at a specific time ($I_{(t)}$), the decay histograms are fitted by convoluting the IRF with a sum of exponential functions to estimate fluorescence decay times (τ_n), shown in Equation (1):

$$I_{(t)} = \sum_n^N A_n e^{-t/\tau_n} \tag{1}$$

The fitted normalized decay histograms for: a) BZO, b) CZO with $N = 2$, and c) SZO with $N = 3$ are presented in **Figure 6**. For BZO, the average photoluminescence lifetimes from three measurements are $\overline{t_1} = 0.29 \pm 0.16$ ns, $\overline{t_2} = 2.43 \pm 0.58$ ns. Similar excited-state and exciton lifetimes in $BaZrO_3$ were previously reported, and decay patterns imply that multiple processes participate in observed emissive exciton decay or radiative transitions.[82] Due to the noise, only a single conclusive spectrum is collected for CZO with estimated $t_1 = 0.13$ ns and $t_2 = 1.23$ ns lifetimes. The 1.23 ns value was reported for CZO, correlated with oxygen vacancies (V_O).[76] In the case of SZO, the average of 4 measurements gives $\overline{t_1} = 0.08 \pm 0.02$ ns, $\overline{t_2} = 0.45 \pm 0.03$ ns, $\overline{t_3} = 1.88 \pm 0.08$ ns. The $\overline{t_1}$ value, significantly shorter than the IRF, is correlated to fast decay processes inside the material. Similar decay timescales were observed for $SrTiO_3$, which luminescence is not solely correlated with bulk V_O, but also with other unidentified intrinsic defects acting as radiative centers.[83] It is important to note that in Figure 6a–c, we observe a significant difference in the signal-to-noise ratio (SNR) comparing the three samples. These measurements have been conducted under identical conditions, highlighting the remarkable SNR exhibited by SZO. Upon analyzing the raw data, the intensity of the SZO surpasses the BZO sample by a factor of 20 and the CZO sample by a factor of 40. This tendency also holds true in wide-field fluorescence images, further supporting the superiority of the SZO sample in excitation efficiency.

Top-view photoluminescence images showcasing the emission from the BZO buckyball, sodalite-inspired architecture, and SZO gyroid upon excitation at 488 nm are presented in Figure 6d–g. The corresponding stop-motion videos presenting z-stack acquisition are also presented (Videos S1–S3, Supporting Information). Figure 6g gives a digital image from the microscope eye-piece showcasing defect-related yellow emission from the SZO gyroid excited at 488 nm. In addition, the photoluminescence (PL) emission spectra are recorded for the 3D BZO, CZO, and SZO microarchitectures using a wide-field microscopy setup at 20× magnification and 415, 450, or 488 nm excitation (Oxxius) (Figure S19, Supporting Information). The emission is filtered using a dichroic mirror with the matched fluorescence filter.

3. Conclusion

Additive manufacturing of 3D-structured perovskite microarchitectures was achieved for the first time using two-photon lithography and tailor-made photoresists. Upon the annealing in the air, the 3D-printed pre-ceramic complex microarchitectures were transformed into the corresponding miniaturized
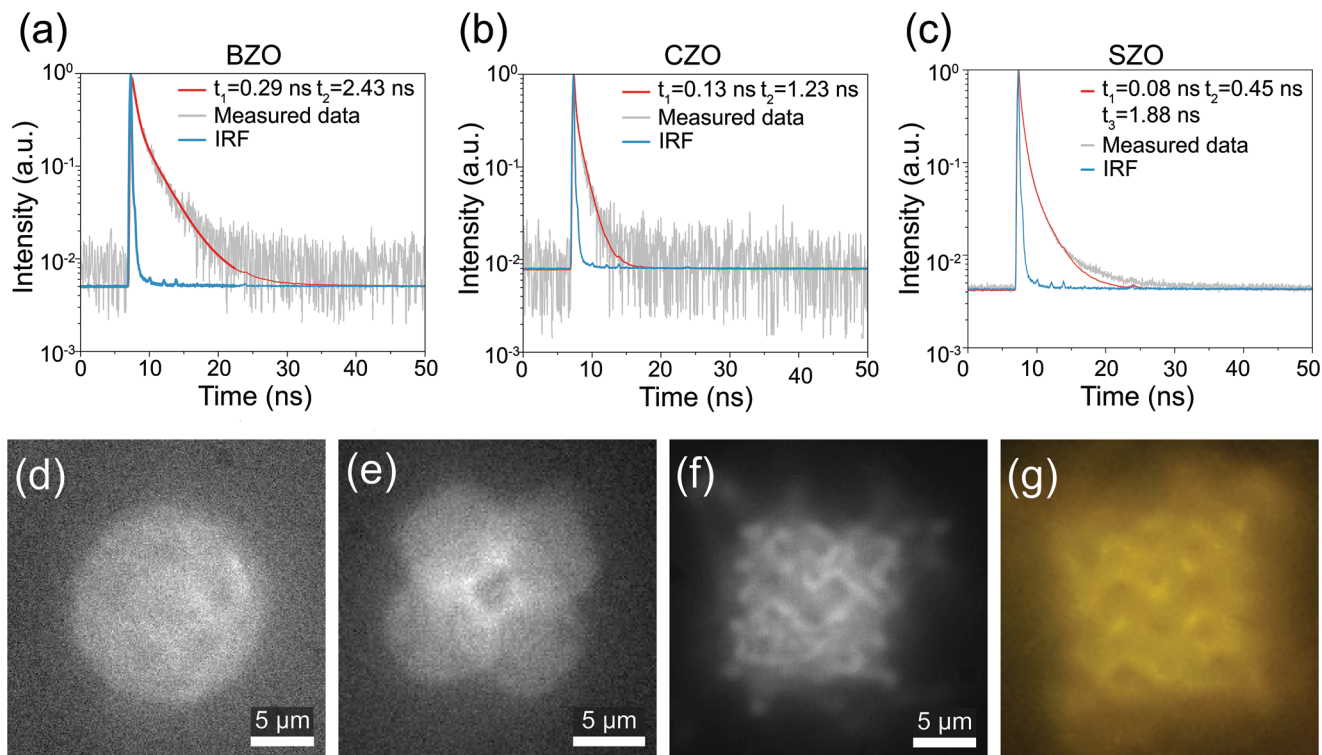
2307077 (9 of 13)

Figure 6. a–c) Normalized PL decay profiles upon 450 nm excitation for BZO (a), CZO (b), and SZO (c) microarchitectures. d–f) Wide-field fluorescence microscopy images of BZO buckyball (d), BZO sodalite-inspired architecture (e), and SZO gyroid (f) upon 488 nm excitation. g) Digital image from the microscope eye-piece presenting yellow emission from the SZO gyroid excited at 488 nm.

perovskite replicas, isotropically shrunken by ≈63%. The effects of the thermal treatment (5 h at 600, 700, 800, 900, and 1000 °C) were studied with XRD. Gradual temperature increases result in the reduced content of impurities, mainly including corresponding sulfates and carbonates with traces of zirconia. Additional characterization with XPS was conducted, confirming the formation of perovskites and the presence of similar impurities on the surface. The synthesis of $BaZrO_3$, $CaZrO_3$, and $SrZrO_3$ was accomplished.

SEM imaging of BZO, CZO, and SZO microarchitectures allowed us to observe crystallites of significantly different grain morphologies. FIB tomography revealed the structural integrity of the representative 3D microarchitectures and enabled the assessment of the homogeneous distribution of Ba/Ca/Sr, Zr, and O throughout the extracted lamellae with EDX. The analysis of BZO, CZO, and SZO lamellae with STEM confirms the formation of $BaZrO_3$, $CaZrO_3$, and $SrZrO_3$. However, a mixed state with ZrO_2 is commonly observed, also evidenced with EDX maps. Visible-range emissions from the manufactured BZO, CZO, and SZO 3D microarchitectures were observed with CL and PL, correlated with various lattice defects, structural order–disorder, and trap states. The PL decay histograms are obtained through TCSPC measurements, enabling the determination of the photoluminescence lifetimes, similar to literature values of $BaZrO_3$, $CaZrO_3$, and $SrZrO_3$.

From a broad perspective, the presented methodology permits the AM of complex 3D-structured mixed oxides, whose chemical composition can be tuned. Our work is the first step toward fabricating dimensionally perovskite microarchitectures, which are significant in photonics, optoelectronics, sensing, and (photo/electro)catalysis.

4. Experimental Section

Materials: Barium acrylate (95%), calcium methacrylate hydrate (95%), and strontium acrylate hydrate (90.5%) were ordered from TCI Europe NV, abcr GmbH, and Gelest, respectively. Isopropanol (ACS reagent, ≥99.5%), methanol (99.9%), pentaerythritol triacrylate (technical grade), and zirconium acrylate were obtained from Sigma-Aldrich. Acrylic acid (99%, stabilized with ≈200 ppm 4-methoxyphenol), dichloromethane (99.9%), and dimethyl sulfoxide (>99%) were acquired from Alfa Aesar. 7-Diethylamino-3-thenoylcoumarin (97%) was acquired from J&K Scientific. All agents were used as received.

Organic–Inorganic Photoresists for Two-Photon Lithography: TPL-compatible photoresists permitting printing precursor photopolymers of BZO, CZO, and SZO suitable for two-photon polymerization (Figures S20 and S21, Supporting Information) with molar absorptivity of 8.78 M^{-1} cm^{-1} were prepared and handled using amber glassware in a yellow-light environment. Acrylic acid (150 mg) was poured into a round bottom flask containing combinations of metal–organic monomers. A fixed amount of zirconium acrylate (37.5 mg) was mixed with barium acrylate (29.5 mg) or strontium acrylate hydrate (27.4 mg), respectively. The zirconium acrylate and calcium methacrylate ratios were precisely adjusted to formulate the recipes yielding the CZO with low side-product quantities (e.g., 37.5 mg ZrA, and 22.4 mg CMH for 1:1 Zr:Ca ratio). To this end, samples with a stoichiometric Zr:Ca ratio and different non-stoichiometric ratios were prepared (i.e., 1:1; 1:1.1; 1:1.25; 1:1.5). To the mixtures, methanol (2 g) and DMSO (500 mg) were added and agitated using a rotary evaporator operated under ambient pressure (40 °C/180 rpm/60 min). After the dissolution of metallic salts, the organic monomer (300 mg), PETA,

was added to the flask, and the mixing continued for 30 min. Afterward, the photoinitiator, DETC (23 mg), and DCM (200 mg) were added. The solution was mixed for 15 min, and later, the pressure was reduced for complete evaporation of MeOH and DCM (40 °C/180 rpm/45 min). The freshly prepared photoresists was used in a TPL process directly.

Two-Photon Lithography and UV Curing: Pre-ceramic architectures (metal-containing polymers) were written on substrates using a commercially available TPL system with an inverse configuration (Photonic GT, Nanoscribe GmbH). The photoresin were drop cast onto glass cover slides (Ø 30 mm) and enclosed between two Kapton tape strips as spacers, on which Si chips (8 × 8 mm) were placed. The printing setup consists of an oil-immersion configuration with a 63× objective lens with numerical aperture NA = 1.4. The system was operated using reflection mode at an average laser power of 23.5 mW and 1 mm s^{-1} scan speed. The peak laser intensity was estimated to be close to 9.64 TW cm^{-2} for these conditions. The two-photon polymerization (TPP) dose was estimated using Equation (2).[79] The estimated TPP dose for each pre-ceramic resin was 53.84 J cm^{-2}. Furthermore, we have estimated that the standard laser source has a central wavelength (λ) at a 780 nm repetition rate 80 MHz (f_{rep}), pulse width 100 fs (τ_L), maximum output power 140 mW, and peak power 25 kW. For high-resolution 3D printing, the focal spot size can be described through the optical lateral resolution (ω_0) and axial resolution (d_x). ω_0 and d_x are shown in Equation (3) and Equation (4). In this case, ω_0 was 278.6 nm, and d_x was 298 nm.[80]

$$D = f_{rep} \tau_L \sqrt{\frac{2}{\pi}} \frac{P_t}{\omega_0 \nu} \tag{2}$$

$$\omega_0 = \frac{\lambda}{2\,NA} \tag{3}$$

$$d_x = \frac{\lambda}{(NA)^2} \tag{4}$$

After conditioning our Nanoscribe system to the previous conditions and printing, the structures were first immersed in DMSO for 2 min and then in MeOH for 5 min to develop to be finally dried with a gentle nitrogen stream. The portions of freshly prepared photoresists non-used during printing were poured into Petri dishes and irradiated with a 36 W halogen UV lamp (365 nm, EBN001, Esperanza) to prepare reference powders in bulk. After ten cycles of 60 min irradiation, the obtained metal–organic photopolymers were ground in an agate mortar and placed into crucibles. The printed structures and UV-cured samples were dried with a nitrogen stream and stored in an oven overnight (ED 23, Binder GmbH) at 80 °C to evaporate traces of DMSO.

Annealing: The 3D-printed microarchitectures and reference powders were placed in open-cap ceramic crucibles to remove the organic constituents from the pre-ceramic polymer and later annealed in an air chamber oven (LH 15/12, Nabertherm). The heating program consisted of a slow heating ramp step (1 °C min^{-1}) to reach 500 °C, followed by a second stage (2 °C min^{-1}) to reach the target temperature (600, 700, 800, 900, or 1000 °C, respectively). The samples were annealed for 5 h and then cooled to room temperature at a natural rate.

X-ray Powder Diffraction: The influence of the annealing conditions on the crystallinity of the yielded powders was characterized using X-ray powder diffraction (XRD). The powdered samples of the UV-cured annealed photoresists were placed on a zero-diffraction substrate and analyzed using an X-ray diffractometer (D2 Phaser, Bruker). The data was acquired within a 20–80° 2θ scan range using a LynxEye detector and Cu-Kα source radiation (30 kV, 10 mA). CrystalSleuth software was used for baseline correction of data.

Scanning Electron Microscopy: The high-resolution images of the printed 3D structures and reference powders were registered using High-Efficiency Electron (HE-SE2) and Inlens detector of the Carl Zeiss, Merlin AURIGA CrossBeam workstation operated at 1.5 kV acceleration voltage.

Scanning Transmission Electron Microscopy: The electron microscopy and chemical analysis were performed in a JEOL ARM-CF Cs corrected microscope, operated at 200 kV, and equipped with an SSD Jeol EDX and a GIF Quantum (Gatan) Dual EELS spectrometer.

Focused Ion Beam Processing and FIB Tomography: The Thermo Scientific Helios 5 UX DualBeam workstation was used to prepare lamellae. The sections of 3D-printed structures were milled using a Ga source, welded to the Cu grid with W, Pt, and C, to be finally thinned and polished using low-energy ions (W, Si). The FIB tomography of BZO and SZO lamellae was performed using Auto Slice & View 4 software; the secondary electron images were recorded at 2 kV acceleration voltage and ≈100 nm slice thickness. In total, 150 frames were recorded for BZO and 74 for SZO. In addition, SEM and STEM images were acquired at 10 kV acceleration voltage.

Energy-Dispersive Spectroscopy: The energy-dispersive spectra were recorded using the EDX attachment to the FIB workstation. The EDX maps were generated using Thermo Scientific Pathfinder X-ray Microanalysis Software. The single pixel size is 100.1 nm; the images were upscaled for display.

Cathodoluminescence: CL measurements were conducted at room temperature with a JEOL JIB-4500 SEM using a Gatan MonoCl4 detector operated at 15 kV acceleration voltage.

Reflectance Spectroscopy (UV–Vis DRS): The BZO, CZO, and SZO reference powders were dispersed in isopropanol and cast on glass slides dropwise. After solvent evaporation, uniform films were obtained, which adhered to the substrate when stored vertically. The UV–vis DRS spectra were collected using a Lambda 950 S (Perkin Elmer) spectrometer using a 150 mm InGaAs integrating sphere (Perkin Elmer) and a focusing lens (Melles Griot). The photomultiplier tube and InGaAs detector slits were 4 and 2 nm. The deuterium lamp was changed to tungsten at 319 nm. As a reference, Spectralon (Labsphere) reflectance standard was used.

Photoluminescence: The sample was positioned facing the objective (i.e., with the substrate behind the printed structures) and mounted in the sample holder by attaching the substrate to a glass coverslip (170 µm thickness, 25 mm diameter) with double-sided adhesive tape. The decay histograms were obtained through time-correlated single-photon counting (TCSPC) measurements. The samples were placed on an inverted fluorescence microscope with a 20× objective and excited with a wide-field laser beam emitted by a super-continuum laser (SuperK Extreme EXB-6, NKT) tuned at 450 nm (FWHM ≈ 10 nm). The resulting PL was collected with the same objective and focused onto a SPAD (single photon avalanche diode, PDM-Red, Micro Photon Devices) coupled to a time-resolved photon counting module (HydraHarp400, PicoQuant). The field of view of the detector is 2.5 µm, and its instrument response function (IRF) has a temporal width of ≈200 ps. The decay histograms were fitted, convoluting the IRF with a sum of exponential functions: $I_{(t)} = \sum_n^N A_n e^{-t/\tau_n}$, where τ_n is the fluorescence decay of the nth component.

Wide-Field Fluorescence Microscopy: The sample was positioned facing the objective (i.e., with the substrate behind the printed structures) and mounted in the sample holder by attaching the substrate to a glass coverslip (170 µm thickness, 25 mm diameter) with double-sided adhesive tape. No immersion oil was used. A 60 × 1.40 NA (Nikon, Plan Apo lambda) objective was mounted on a Nikon Ti Eclipse 2 microscope body. The excitation was generated using a 488 nm laser (Oxxius, LBX-488-100) with 200 W cm^{-2} irradiance. The emission was separated from the excitation and filtered by a quad-based 405/488/561/647 nm dichroic mirror with the matched fluorescence filter (Semrock). The detection path consisted of an afocal to adapt the magnification and an sCMOS camera (Photometrics Prime 95B). The exposure was set to 30 ms, and the pixel size in the object plane was 110 nm. The 3D images were acquired by capturing z-stacks. The axial displacement was achieved using a piezoelectric nanopositioner (PI), and one 300 ms exposure frame was recorded each 500 nm.

X-ray Photoelectron Spectroscopy: The XPS analysis of the BZO, CZO, and SZO reference powders was conducted with a scanning XPS/HAXPES microprobe (PHI Quantes). An Al Kα source (1486.6 eV; 25 W, 15 kV) of 100 µm spot size was used. The general survey and core spectra were collected using 280 eV and 112 pass energies, with 1 and 0.1 eV steps, respectively. The synthetic Voigt peaks were generated using the CasaXPS

package to deconvolute the spectra; Tougaard and Shirley background types were used. The core spectra are calibrated to the position of the aliphatic carbon peak (C–C, C–H) at 284.8 eV.

Supporting Information

Supporting Information is available from the Wiley Online Library or from the author.

Conflict of Interest

The authors declare no conflict of interest.

Data Availability Statement

The data that support the findings of this study are available from the corresponding author upon reasonable request.

[1] Z. Zeng, Y. Xu, Z. Zhang, Z. Gao, M. Luo, Z. Yin, C. Zhang, J. Xu, B. Huang, F. Luo, Y. Du, C. Yan, *Chem. Soc. Rev.* **2020**, *49*, 1109.

[2] M. Johnsson, P. Lemmens, in *Handbook of Magnetism and Advanced Magnetic Materials* (Ed.: H Kronmüller, S. Parkin, M. Coey, A. Inoue), John Wiley & Sons, Ltd, Chichester, UK **2007**.

[3] M. A. Peña, J. L. G. Fierro, *Chem. Rev.* **2001**, *101*, 1981.

[4] P. Kanhere, Z. Chen, *Molecules* **2014**, *19*, 19995.

[5] A. Kumar, A. Kumar, V. Krishnan, *ACS Catal.* **2020**, *10*, 10253.

[6] N. N. Greenwood, A. Earnshaw, in *Chemical Elements* (Eds.: N. N. Greenwood, A. Earnshaw), Butterworth-Heinemann, Oxford, UK **1997**.

[7] S. A. Cotton, *Annu. Rep. Prog. Chem. Sect. A: Inorg. Chem.* **1997**, *93*, 143.

[8] G. Balcas, M. Malinauskas, M. Farsari, S. Juodkazis, *Adv. Funct. Mater.* **2023**, *33*, 2215230.

[9] S. Parida, S. K. Rout, V. Subramanian, P. K. Barhai, N. Gupta, V. R. Gupta, *J. Alloys Compd.* **2012**, *528*, 126.

[10] M.-H. Lin, M.-C. Wu, C.-Y. Huang, C.-H. Lin, T.-Y. Tseng, *J. Phys. D Appl. Phys.* **2010**, *43*, 295404.

[11] S. Parida, S. K. Rout, L. S. Cavalcante, E. Sinha, M. S. Li, V. Subramanian, N. Gupta, V. R. Gupta, J. A. Varela, E. Longo, *Ceram. Int.* **2012**, *38*, 2129.

[12] A. K. Kunti, N. Patra, R. A. Harris, S. K. Sharma, D. Bhattacharyya, S. N. Jha, H. C. Swart, *Inorg. Chem. Front.* **2021**, *8*, 821.

[13] A. M. Huerta-Flores, F. Ruiz-Zepeda, C. Eyovge, J. P. Winczewski, M. Vandichel, M. Gaberscek, N. D. Boscher, H. J. G. E. Gardeniers, L. M. Torres-Martínez, A. Susarrey-Arce, *ACS Appl. Mater. Interfaces* **2022**, *14*, 31767.

[14] Z. Kang, B. Yu, S. Fu, D. Li, X. u. Zhang, Z. Qian, Z. Zhong, B. Yu, H. Ding, Y. Zhu, J. Huang, *Appl. Mater. Today* **2019**, *16*, 132.

[15] H. Cui, R. Hensleigh, D. Yao, D. Maurya, P. Kumar, M. G. Kang, S. Priya, X. R. Zheng, *Nat. Mater.* **2019**, *18*, 234.

[16] V. V. Vogler-Neuling, R. Savo, D. Pohl, N. R. Hendricks, L. Lang, M. Timofeeva, B. Schneider, F. U. Richter, F. Timpu, S. Monneret, F. Starsich, R. Grange, *Phys. Status Solidi B* **2020**, *257*, 1900755.

[17] H. Chen, J. Wang, S. Peng, D. Liu, W. Yan, X. Shang, B. Zhang, Y. Yao, Y. Hui, N. Zhou, *Nano-Micro Lett.* **2023**, *15*, 180.

[18] A. Marino, J. Barsotti, G. De Vito, C. Filippeschi, B. Mazzolai, V. Piazza, M. Labardi, V. Mattoli, G. Ciofani, *ACS Appl. Mater. Interfaces* **2015**, *7*, 25574.

[19] X. Wen, B. Zhang, W. Wang, F. Ye, S. Yue, H. Guo, G. Gao, Y. Zhao, Q. Fang, C. Nguyen, X. Zhang, J. Bao, J. T. Robinson, P. M. Ajayan, J. Lou, *Nat. Mater.* **2021**, *20*, 1506.

[20] A. Desponds, A. Banyasz, D. Chateau, A. Tellal, A. Venier, S. Meille, G. Montagnac, J. Chevalier, C. Andraud, P. L. Baldeck, S. Parola, *Small* **2021**, *17*, 2102486.

[21] F. Kotz, A. S. Quick, P. Risch, T. Martin, T. Hoose, M. Thiel, D. Helmer, B. E. Rapp, *Adv. Mater.* **2021**, *33*, 2006341.

[22] H. Wang, W. Zhang, D. Ladika, H. Yu, D. Gailevicius, H. Wang, C.-F. Pan, P. N. S. Nair, Y. Ke, T. Mori, J. Y. E. n. Chan, Q. Ruan, M. Farsari, M. Malinauskas, S. Juodkazis, M. Gu, J. K. W. Yang, *Adv. Funct. Mater.* **2023**, *33*, 2214211.

[23] A. Vyatskikh, R. C. Ng, B. Edwards, R. M. Briggs, J. R. Greer, *Nano Lett.* **2020**, *20*, 3513.

[24] J. Winczewski, M. Herrera, C. Cabriel, I. Izeddin, S. Gabel, B. Merle, A. Susarrey Arce, H. Gardeniers, *Adv. Opt. Mater.* **2022**, *10*, 2102758.

[25] D. W. Yee, M. L. Lifson, B. W. Edwards, J. R. Greer, *Adv. Mater.* **2019**, *31*, 1901345.

[26] X. Xia, Q. i. Chen, C. Tsay, C. B. Arnold, C. K. Madsen, *Opt. Lett.* **2010**, *35*, 1695.

[27] J. Bauer, C. Crook, T. Baldacchini, *Science* **2023**, *380*, 960.

[28] D. Gailevicius, V. Padolskyte, L. Mikoliunaite, S. Sakirzanovas, S. Juodkazis, M. Malinauskas, *Nanoscale Horiz.* **2019**, *4*, 647.

[29] A. Desponds, A. Banyasz, G. Montagnac, C. Andraud, P. Baldeck, S. Parola, *J. Sol–Gel Sci. Technol.* **2020**, *95*, 733.

[30] L. Brigo, J. E. M. Schmidt, A. Gandin, N. Michieli, P. Colombo, G. Brusatin, *Adv. Sci.* **2018**, *5*, 1800937.

[31] H. Dory, P. Miele, C. Salameh, *Int. J. Appl. Ceram. Technol.* **2023**, *20*, 141.

[32] T. A. Pham, D.-P. Kim, T.-W. Lim, S.-H. Park, D.-Y. Yang, K.-S. Lee, *Adv. Funct. Mater.* **2006**, *16*, 1235.

[33] Q. Hanniet, E. Petit, S. Calas-Etienne, P. Etienne, K. Aissou, C. Gervais, P. Miele, B. Charlot, C. Salameh, *Mater. Des.* **2022**, *223*, 111234.

[34] I. Cooperstein, S. R. K. C. Indukuri, A. Bouketov, U. Levy, S. Magdassi, *Adv. Mater.* **2020**, *32*, 2001675.

[35] J. Winczewski, M. Herrera, H. Gardeniers, A. Susarrey-Arce, *Chem. Commun.* **2023**, *59*, 3095.

[36] T. Yu, C. H. Chen, X. F. Chen, W. Zhu, R. G. Krishnan, *Ceram. Int.* **2004**, *30*, 1279.

[37] A. Dwivedi, A. N. Cormack, *J. Solid State Chem.* **1989**, *79*, 218.

[38] X. Meng, E. Li, W. Huang, Y. u. Bai, W. Ma, R. Wang, *Surf. Coat. Technol.* **2019**, *369*, 87.

[39] P. Ptáček, E. Bartoníčková, J. Švec, T. Opravil, F. Soukal, F. Frajkorová, *Ceram. Int.* **2015**, *41*, 115.

[40] K. S. P. Karunadasa, C. H. Manoratne, H. M. T. G. A. Pitawala, R. M. G. Rajapakse, *J. Phys. Chem. Solids* **2019**, *134*, 21.

[41] In *Thermal Decomposition of Ionic Solids: Chemical Properties and Reactivities of Ionic Crystalline Phases*, (Eds.: M. E. B. Andrew, K. Galwey), Elsevier Science, Amsterdam, The Netherlands **1999**.

[42] J. P. Winczewski, S. Zeiler, S. Gabel, A. Susarrey-Arce, J. G. E. Gardeniers, B. Merle, *Mater. Des.* **2023**, *232*, 112142.

[43] R. S. André, S. M. Zanetti, J. A. Varela, E. Longo, *Ceram. Int.* **2014**, *40*, 16627.

[44] S. M. Hope, S. Kundu, C. Roy, S. S. Manna, A. Hansen, *Front. Phys.* **2015**, *3*, 72.

[45] M. Pelanconi, M. Barbato, S. Zavattoni, G. L. Vignoles, A. Ortona, *Mater. Des.* **2019**, *163*, 107539.

[46] C. Xie, D. Yan, H. Li, S. Du, W. Chen, Y. Wang, Y. Zou, R. Chen, S. Wang, *ACS Catal.* **2020**, *10*, 11082.

[47] S. Cao, F. F. Tao, Y. u. Tang, Y. Li, J. Yu, *Chem. Soc. Rev.* **2016**, *45*, 4747.

[48] B. Koo, K. Kim, J. K. Kim, H. Kwon, J. W. Han, W. Jung, *Joule* **2018**, *2*, 1476.

[49] G. Taglieri, M. Tersigni, P. L. Villa, C. Mondelli, *Int. J. Inorg. Mater.* **1999**, *1*, 103.

[50] P. Makula, M. Pacia, W. Macyk, *J. Phys. Chem. Lett.* **2018**, *9*, 6814.

[51] L. S. Cavalcante, V. M. Longo, M. Zampieri, J. W. M. Espinosa, P. S. Pizani, J. R. Sambrano, J. A. Varela, E. Longo, M. L. Simões, C. A. Paskocimas, *J. Appl. Phys.* **2008**, *103*, 063527.

[52] A. B. Lavand, Y. S. Malghe, *J. Therm. Anal. Calorim.* **2014**, *118*, 1613.

[53] P. Stoch, J. Szczerba, J. Lis, D. Madej, Z. Pedzich, *J. Eur. Ceram. Soc.* **2012**, *32*, 665.

[54] Z. F. Hou, *Phys. B: Condens. Matter* **2008**, *403*, 2624.

[55] K. Hkiri, H. E. A. Mohamed, B. S. Khanyile, C. Mtshali, M. Nkosi, M. Ben Salem, M. Maaza, M. Zouaoui, *Surf. Interfaces* **2021**, *25*, 101259.

[56] L. S. Cavalcante, A. Z. Simões, J. C. Sczancoski, V. M. Longo, R. Erlo, M. T. Escote, E. Longo, J. A. Varela, *Solid State Sci.* **2007**, *9*, 1020.

[57] A. M. Huerta-Flores, L. M. Torres-Martínez, D. Sánchez-Martínez, M. E. Zarazúa-Morín, *Fuel* **2015**, *158*, 66.

[58] I. I. Leonidov, V. I. Tsidilkovski, E. S. Tropin, M. I. Vlasov, L. P. Putilov, *Mater. Lett.* **2018**, *212*, 336.

[59] B. Henderson, *Contemp. Phys.* **2002**, *43*, 273.

[60] C. F. Klingshirn, *Semiconductor Optics*, Springer, Berlin/Heidelberg, Germany **2012**.

[61] L. S. Cavalcante, J. C. Sczancoski, J. W. M. Espinosa, V. R. Mastelaro, A. Michalowicz, P. S. Pizani, F. S. De Vicente, M. S. Li, J. A. Varela, E. Longo, *J. Alloys Compd.* **2009**, *471*, 253.

[62] H. Abdou, S. K. Gupta, Y. Mao, *J. Lumin.* **2019**, *214*, 116599.

[63] L. R. Macario, M. L. Moreira, J. Andrés, E. Longo, *CrystEngComm* **2010**, *12*, 3612.

[64] E. C. Aguiar, A. Z. Simões, C. A. Paskocimas, M. Cilense, E. Longo, J. A. Varela, *J Mater Sci* **2015**, *26*, 1993.

[65] V. H. Romero, E. De La Rosa, P. Salas, J. J. Velázquez-Salazar, *J. Solid State Chem.* **2012**, *196*, 243.

[66] M. Boffelli, W. Zhu, M. Back, G. Sponchia, T. Francese, P. Riello, A. Benedetti, G. Pezzotti, *J. Phys. Chem. A* **2014**, *118*, 9828.

[67] J.-M. Costantini, Y. Watanabe, K. Yasuda, M. Fasoli, *J. Appl. Phys.* **2017**, *121*, 153101.

[68] M. L. Moreira, J. Andrés, J. A. Varela, E. Longo, *Cryst. Growth Des.* **2009**, *9*, 833.

[69] K. h. Dhahri, M. Bejar, E. Dhahri, M. J. Soares, M. F. P. Graça, M. A. Sousa, M. A. Valente, *Chem. Phys. Lett.* **2014**, *610–611*, 341.

[70] Z. Wang, J. Zhang, G. Zheng, X. Peng, H. Dai, *J. Lumin.* **2013**, *144*, 30.

[71] C. Kayathiri, A. R. Balu, M. Suganya, G. Vinitha, Z. Delci, S. Balamurugan, M. Karthika, S. Anitha, A. Prabavathi, *Mater. Sci. Eng., B* **2022**, *278*, 115636.

[72] N. Li, K. Tong, L. Yang, X. Du, *Mater. Today Energy* **2022**, *29*, 101100.

[73] J. M. Aguirre-Cortés, A. I. Moral-Rodríguez, E. Bailón-García, A. Davó-Quiñonero, A. F. Pérez-Cadenas, F. Carrasco-Marín, *Appl. Mater. Today* **2023**, *32*, 101831.

[74] J. J. Carey, K. P. Mckenna, *J. Phys. Chem. C* **2019**, *123*, 22358.

[75] D. N. Mueller, M. L. Machala, H. Bluhm, W. C. Chueh, *Nat. Commun.* **2015**, *6*, 6097.

[76] S. K. Gupta, P. S. Ghosh, N. Pathak, R. Tewari, *RSC Adv.* **2015**, *5*, 56526.

[77] X. Liu, J. Zhang, X. Ma, H. Sheng, P. Feng, L. Shi, R. Hu, Y. Wang, *J. Alloys Compd.* **2013**, *550*, 451.

[78] V. M. Longo, L. S. Cavalcante, R. Erlo, V. R. Mastelaro, A. T. De Figueiredo, J. R. Sambrano, S. De Lázaro, A. Z. Freitas, L. Gomes, N. D. Vieira, J. A. Varela, E. Longo, *Acta Mater.* **2008**, *56*, 2191.

[79] V. M. Longo, L. S. Cavalcante, M. G. S. Costa, M. L. Moreira, A. T. De Figueiredo, J. Andrés, J. A. Varela, E. Longo, *Theor. Chem. Acc.* **2009**, *124*, 385.

[80] D. J. Lee, D. H. Kim, J. W. Park, Y. S. Lee, *J. Korean. Phys. Soc.* **2011**, *59*, 2797.

[81] D. Kan, T. Terashima, R. Kanda, A. Masuno, K. Tanaka, S. Chu, H. Kan, A. Ishizumi, Y. Kanemitsu, Y. Shimakawa, M. Takano, *Nat. Mater.* **2005**, *4*, 816.

[82] A. S. Patra, G. Gogoi, M. Qureshi, *ACS Omega* **2018**, *3*, 10980.

[83] A. Rubano, D. Paparo, F. M. Granozio, U. Scotti Di Uccio, L. Marrucci, *J. Appl. Phys.* **2009**, *106*, 103515.